AUTHOR QUERY FORM

	Journal: Discrete Applied Mathematics Article Number: 9237	Please e-mail your responses and any corrections to: E-mail: corrections.esch@elsevier.river-valley.com
ELSEVIER		

Dear Author,

Please check your proof carefully and mark all corrections at the appropriate place in the proof (e.g., by using on-screen annotation in the PDF file) or compile them in a separate list. Note: if you opt to annotate the file with software other than Adobe Reader then please also highlight the appropriate place in the PDF file. To ensure fast publication of your paper please return your corrections within 48 hours.

For correction or revision of any artwork, please consult http://www.elsevier.com/artworkinstructions.

Your article is registered as belonging to the Special Issue/Collection entitled "DGA13". If this is NOT correct and your article is a regular item or belongs to a different Special Issue please contact s.shanmugam@elsevier.com immediately prior to returning your corrections.

Location in article	Query / Remark click on the Q link to go Please insert your reply or correction at the corresponding line in the proof
Q1	Please confirm that given names and surnames have been identified correctly.
Q2	Please check the e-mail address(es) of the author(s).
Q3	Color statement has been added to the caption(s) of Figs. 1 and 6–9. Please check, and correct if necessary.
Q4	Please check the word "underling"and correct if necessary.
Q5	The decimal comma has been changed to a decimal point in Table 1 (2 cases). Please check, and correct if necessary.
Q6	Please check the edits made in this section, and correct if necessary.
Q7	Please provide grant number for 'FAPERJ'.
	Please check this box or indicate your approval if you have no corrections to make to the PDF file ☐

Thank you for your assistance.

Discrete Applied Mathematics xx (xxxx) xxx–xxx

Contents lists available at ScienceDirect

Discrete Applied Mathematics

journal homepage: www.elsevier.com/locate/dam

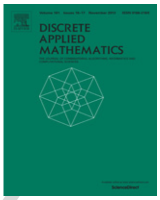

A new measure for comparing biomedical regions of interest in segmentation of digital images

Q1 Aura Conci [a,*], Stephenson S.L. Galvão [a], Giomar O. Sequeiros [a], Débora C.M. Saade [a], Trueman Machenry [b]

[a] Computer Institute, Fluminense Federal University, Brazil

[b] Department of Mathematics and Statistics, York University, Canada

A R T I C L E I N F O

Article history:
Received 5 January 2014
Received in revised form 30 May 2015
Accepted 4 June 2015
Available online xxxx

Keywords:
Biomedical image processing
Image segmentation
Infrared imaging
Hausdorff distance
Discrete sets

A B S T R A C T

The segmentation of the region of interest (ROI) of digital images is generally the first step in the pattern recognition (PR) procedure. Automatic segmentation of biomedical images is desirable and comparisons among new approaches, by using available databases, are important. We present a new approach to compute the Hausdorff distance (HD) between digital images. Although HD is the most used distance estimator among sets, we show why it is not suitable for biomedical applications. In this paper, a new technique to define the degree of correction of the ROI is developed to serve as a basis for the comparisons used to validate works on segmentation of biomedical images. As for online diagnosis, the comparison among possible techniques must be efficient enough to: (1) be done in real time (i.e. during the examination), (2) allow the inclusion of priority aspects, and (3) be intuitive and simple enough to be easily followed by people with no computational or mathematical background. We develop a new index by considering the expectations of the medical doctors who are using computer systems for diagnostic aids, and take into consideration how these systems use ROIs to extract feature properties from the examinations. We discuss conditions for empirically defining a measure for calculating similarities and differences between ROIs. The proposed method is applied to both real and simulated data examples.

1. Introducing the problem

Dedicated digital image processing chips convert raw data acquired from digital cameras into a discrete set of points. Q2 The quality of the digital images is related to the numbers of discrete points used (named *pixels* in computer graphics and in image processing) and to the resolution used by the digital camera. Image processing is typically a special application of methods from discrete mathematics [9]; it considers several tools to manipulate the images in many ways. In this work we are interested in a particular type of digital camera that can acquire the infrared (IR) frequency of each discrete point in a scene (Fig. 1(a)). Even moreparticularly, we are interested in the relationship with this IR frequency and the temperature of Q3 the human body, when such an element is included in the frame (Fig. 1(b)). We consider that, for each discrete point that is captured, we have its coordinates as well as its temperature, which is a real number representing a color and able to take a finite number of different values (Fig. 1(a) and (c)). These temperatures of the human body can be used for diagnosis, where

* Corresponding author.
E-mail addresses: aconci@ic.uff.br (A. Conci), sgalvao@ifpi.edu.br (S.S.L. Galvão), goliver@ic.uff.br (G.O. Sequeiros), debora@ic.uff.br (D.C.M. Saade), machenry@mathstat.yorku.ca (T. Machenry).

http://dx.doi.org/10.1016/j.dam.2015.06.002

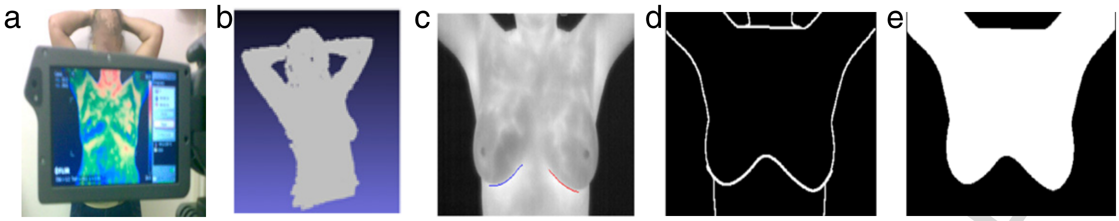

Fig. 1. IR camera and the captured scene, where the temperature of each discrete point is represented by colors (a), each discrete point of the image (b), representation of the temperature using gray level and the first step of segmentation process (c), that is, the inframammary folds of the right and left breast of the patient defined by blue and red lines respectively. Two possible ways to define the ROI are by its boundaries (d) and, by labeling the pixels belonging to ROI (e). (For interpretation of the references to color in this figure legend, the reader is referred to the web version of this article.)

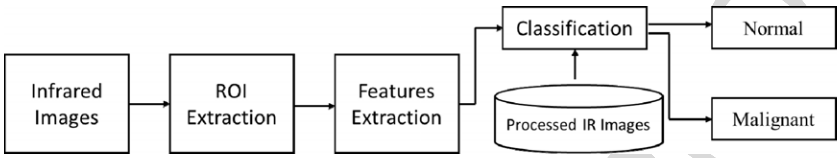

Fig. 2. Steps of IR based CADs for breast diseases.

the temperatures are restricted to a special region of the body. Proper definition of such a region is very important for the following steps of the application. When algorithms define these boundaries, the distances among the correct borders, and those achieved by a given implementation, need to be characterized. The Hausdorff distance (HD) is a metric for evaluating the distance between discrete sets of points [2]. This paper presents a new algorithm for HD computation for discrete images, based on the geometry of parallel bodies [5], and the characterization of the distance among sets of points [11].

Pattern Recognition (PR) and image processing techniques have been applied in analysis of the most common types of medical diagnosis [16]. In these techniques, the first step after acquiring the image (Fig. 2) is to separate the important elements, that is, to obtain the region of interest (ROI) [19]. Two common representations of the ROI are by its boundary or by its area. A contrasting line can be used in the graphical representation of ROI in the first case (Fig. 1(d)). In the second case, the ROI can be identified by labeling its pixels as "1" or white (Fig. 1(e)). In the IR frontal breast examination, right and left orientation always refers to the patient. Thus, in Fig. 1(c), a blue line defines the lower boundary (inframammary fold) of right side of the patient, and a red line defines the lower boundary of the left breast.

Typically, there are two ways to design image segmentation algorithms, with user interactions or automatically. In the first case, there is some degree of dialog with the user, for instance, in the identification of the important objects in the image. In the second case, the segmentation is realized without any human intervention. In most of the cases of computer aided diagnosis (CAD), a complete automatic procedure of ROI segmentation must be carried out [7]. That is, this region must be found with no user interaction. However, due to the complexity and importance of proper ROI definition for the next steps of these CAD systems (that are represented in Fig. 2), the exactitude of ROI identification algorithms must be proved. To evaluate the ROI correctness, a large number of cases, which are segmented by a group of experts, needs to be considered. However, it is not easy to find and persuade good specialists to spend their time doing this type of work. In addition, more than one result for each case and image is needed in order to achieve segmentations free of personal bias. These aspects make the set of segmentations considered to be correct of great value in the research. They constitute the commonly named "truest sets" for comparisons of results, or what is called the "ground truth" (GT) [4,6].

After a number of automatic segmentations have passed through the comparison stage with the GT (composed by a combination of correct segmentations), they are included in CAD systems. Moreover, these systems, in most cases, perform segmentation algorithms in real time, that is, during the patient examination period. In this way, in case of doubt, there is the possibility of repeating the examination process. In order to verify the adequacy of different approaches, numerical (rather than visual) techniques must be used to compare the ROIs. Keeping in mind all these aspects, it is clear why it is of great importance to have a metric to show how similar two ROI boundaries are. The definition of a fast, intuitive and correct evaluator for medical ROI comparisons is still an open problem. The presentation of a new index to compare ROIs for diagnostic systems is the goal of this work. It also presents a brief review of similarity measures currently used for ROI comparison. Moreover, it develops a new candidate for a measure with which to compare nonconvex, nondisjoint, but fully connected regions, that constitute the ROI of IR breast images, and discusses its advantages.

This work is based on an application under development in the Radiologic Service of the University Hospital of the Fluminense Federal University (UFF), Niteroi, Rio de Janeiro, Brazil: The project PROENG (http://visual.ic.uff.br/en/proeng/). The aim of this project is to research the possibilities of IR breast examinations to help breast disease detection, and to develop a methodology for machine learning and decision support system for the early detection of breast cancer and follow-up by adjuvant therapy.

The rest of the paper is organized as follows. The next section gives the reader some background about the importance of ROI validation. In Section 3, we consider details of our new index and other measure to compare segmentation approaches.

Please cite this article in press as: A. Conci, et al., A new measure for comparing biomedical regions of interest in segmentation of digital images, Discrete Applied Mathematics (2015), http://dx.doi.org/10.1016/j.dam.2015.06.002

Here the new algorithm for HD is presented. Results and comparison are discussed in Section 4. Section 5 concludes the paper.

2. Validation of the segmentation results

Image segmentation is the procedure of extracting particular structures of interest (e.g., breast tissue) from an image (e.g., mammogram). Before an algorithm for segmentation can be used clinically (or commercially), it is imperative to know how well the algorithm performs on a wide range of real images, comprising possibly hundreds of test cases. If a GT set is available for each of these test cases (e.g., manual segmentations from clinicians) then it is possible to use these segmentations as a basis to evaluate the segmentation performance of the algorithm. However, for any clinical task, it is possible to have a range of good segmentations (e.g., two clinicians can provide slightly different segmentations), at the same time, it is possible that even seemingly small deviations from the GT can have great clinical importance. Consequently, a visual inspection is often necessary to assess whether differences between segmentations are medically significant.

In the development of CADs, a lot of time and effort are spent in order to evaluate image segmentation algorithms. If an algorithm does not provide accurate enough results from a medical diagnostic point of view, this is considered unacceptable, and the computer science expert needs to modify it and re-run the whole test suite until it achieves good results. This process is repeated until the image segmentation algorithm evolves to its final acceptable version, where it passes properly into the test suite. However, this evaluation process is mostly done visually. It is very time consuming, requiring the presence of reliable experts from the medical area being studied.

The main reason for this is that segmentation methodologies are very dependent on the underling application. There is no standard for all cases, and it must be evaluated for each new application. The evaluation is more efficient when a GT is used for comparison with the result of the algorithm in analysis. The degree of error must be evaluated by using some measure to compare the results obtained by diverse techniques with an expert validation. Once a valid measure is found, the results produced by any new version of the image segmentation algorithm can be tested in a simpler way, deemed correct or incorrect depending on whether or not it is consistent with the segmentations previously deemed correct (the GT). In this way, because there is not human intervention to validate the results, substantial saving can be obtained during testing. Q4

Image quality measures play important roles in a broad range of applications of image processing and analysis. Image acquisition, compression, communication, restoration, enhancement, display, printing, watermarking and PR are some examples. The most widely used reference of the similarity between an image A and an image B are based on their correlations, or in the assessment of peak signal-to-noise ratio (PSNR) of the difference between the images (i.e. $|A - -B|$), or in its mean squared error (MSE). Although, PSNR matches the human perception better than the other [24,25], all of them are more representative of image quality, and inadequate for evaluation of image segmentation results.

There is no specific way of knowing which measures allow proper comparison of two segmentations in all applications. Medical imaging is related to what is clinically relevant for a particular segmentation task. The ROI segmentation in IR images is intended to separate the regions of the breast from the rest of the image. The breast is made up of connective tissue, fat, and tissue that contain the glands that produce milk. It also contains blood and lymph vessels. The lymph vessels carry fluid (the lymph) that helps in case of infections and other diseases. Lymph nodes are small bean-shaped structures that are found throughout the body. They filter substances in lymph. Clusters of lymph nodes are found near the breast in the axillary region (that is under the arm), above the collarbone, and in the chest. About 75% of lymph from the breasts drains into the lymph nodes, making them important in the diagnosis of breast cancer. For this, the ROI must include these regions. That is, the extraction (from the acquired images) of the ROI must include all breast tissue, and, as much as possible, all the related ganglion groups [14,3].

Fig. 3 considers ROI (dark gray)and GT (light gray)area overlapped for comparison. For this evaluation, we denote by: True Positive (***TP***) the white pixels belonging to the ROI of the GT classified correctly as in the ROI by the segmentation procedure; True Negative (***TN***) those black pixels outside of the ROI area of the GT that are classified correctly as in this condition. The label False Positive (***FP***) is assigned to pixels not in ROI of the GT but classified as in the ROI for the approach, that is, classified incorrectly as positive (in the ROI region). The False Negative (***FN***) denotes the pixels that pertain to the ROI of the GT incorrectly classified as out of the ROI.

Accuracy (***ACC***), sensitivity (***SEN***), specificity (***ESP***), positive predictive (***PDP***) and negative predictive (***PDN***) were estimated using the ***TP***, ***TN***, ***FP*** and ***FN*** values [15]. They are measured by (1)–(5):

$$ACC = (TP + TN)/(FN + FP + TN + TP) \tag{1}$$

$$SEN = TP/(TP + FN) \tag{2}$$

$$ESP = TN/(TN + FP) \tag{3}$$

$$PDP = TP/(TP + FP) \tag{4}$$

$$PDN = TN/(TN + FN). \tag{5}$$

Usually all of (1)–(5) are used to compare segmentation results. This great number of values makes the comparisons rather complex. To simplify, combinations of these have been proposed, as the Efficiency (***EFI***) and Youden index

Please cite this article in press as: A. Conci, et al., A new measure for comparing biomedical regions of interest in segmentation of digital images, Discrete Applied Mathematics (2015), http://dx.doi.org/10.1016/j.dam.2015.06.002

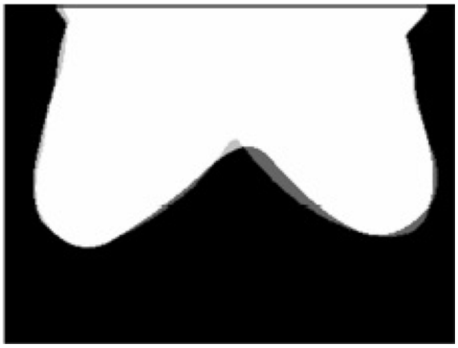

Fig. 3. Overlapping automatic segmentation (dark gray)and GT (light gray).

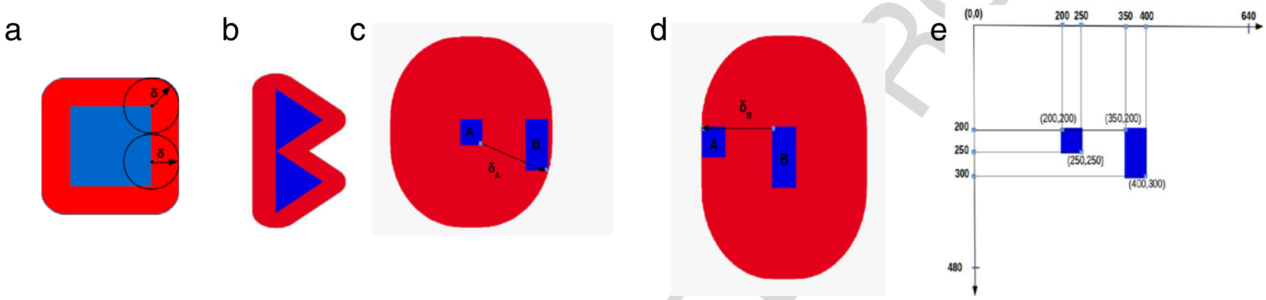

Fig. 4. Parallel body for a square (a) and a non convex set (b). The construction of the smallest δ-*parallel body* of A contains B (c) and vice–versa (d). A and B represented in a coordinate system for computation of HD(A,B) by the max $\{\delta_A, \delta_B\}$ (e).

(***Y-index***) [23]:

$$EFI = 1/2(SEN + ESP)$$

$$Y\text{-}index = (SEN + ESP - 1).$$

From Fig. 1 (d) and Fig. 3, it seems that the distance between each curve of the border can be a possible measure of ROIs closeness. However, as they are discrete sets the comparison must be made between sets of points defining each boundary (i.e. the border of the areas in Fig. 3). The following section considers this approach.

3. Hausdorff distance and new approaches for ROI comparison

Let D be a closed subset of R^n, and let S denote the class of all nonempty compact subsets of D. Capital letters (e.g. A and B) are used to denote sets and the lower case letters (e.g. x and y) represent points. We use the notation $|x|$ to describe the norm of a point on R or on R^2, where $x = (x_1, x_2)$. Set operations are calculated related to the domain D. For a set A, A^c and ∂A denotes its complement and its boundary. The difference between sets A and B is $A \backslash B = \{x \in D : \ x \in A \text{ and } x \notin B\}$, so $A^c = D \backslash A$.

The HD (or the *Hausdorff metric*) measures how far two sets, in a metric space, are from each other [1]. The alternative way of defining the HD using the geometry of a proper δ-*parallel body* of $A \in S$ is very intuitive, and is the definition used here. The *parallel body* of $A \in S$, A_δ, is given by [5, p. 4]:

$$A_\delta = \{x \in D : \ |x - a| \leq \delta \text{ for some a } \in A\}. \tag{6}$$

Fig. 4 shows the construction of the parallel body for a convex (Fig. 4(a)) and non convex set (Fig. 4(b)), when the Euclidean metric is used in R^2. The geometry of A_δ is related with the *shape* of A and with the *local neighborhoods* of the metric space under consideration [17, p. 86].

The HD between two sets A, B is the least δ such that the δ-*parallel body* of A, A_δ, contains B and the δ-*parallel body* of B, B_δ, contains A [5, p. 114]. That is HD between A and B is:

$$HD(A, B) = inf\{\delta : \ A \subset B_\delta \text{ and } B \subset A_\delta\}. \tag{7}$$

The smallest δ-parallel body of A containing B and the smallest δ-parallel body of B containing A, are represented in Fig. 4(c) and (d). Fig. 4(e) illustrates how expression (7) can be used for the computation of the HD between A and B.

It is readily verified that HD(A,B) is a metric for S [5, p. 114]. It is possible to see that $A \subset B_\delta$ when the $A \backslash B_\delta$ is the empty set. Thus

$$HD(A, B) = inf\{\delta : A \backslash B_\delta = \emptyset \text{ and } B \backslash A_\delta = \emptyset\}. \tag{8}$$

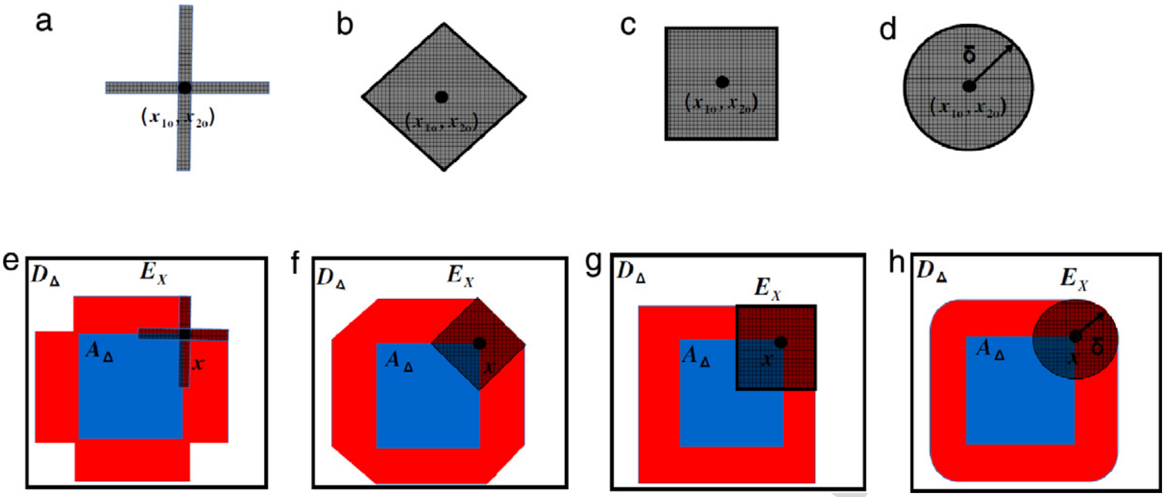

Fig. 5. Some structuring element E with center marked in black (a–d) and dilation of the same set by each E (e–h).

Considering the definition of the *closure of* A and B, denoted *by* A^- and B^- [10, p. 114] we have:

$$HD(A^-, B^-) = \inf\{\delta : A^- \subset B^-_\delta \text{ and } B^- \subset A^-_\delta\} = \inf\{\delta : A \subset B_\delta \text{ and } B \subset A_\delta\} = HD(A, B). \tag{9}$$

Moreover, by definition of the boundary of A and B: ∂A and ∂B [10, p. 181] we have:

$$HD(\partial A, \partial B) = HD(A^-, B^-) = HD(A, B). \tag{10}$$

A discrete subset of a metric space is a set containing isolated points only; every finite set is therefore discrete. In expression (9), it is plausible to replace the set A with a discrete subset A_Δ representing A. Let ∂A_Δ be $A_\Delta \cap \partial A$. Notice that ∂A_Δ does not correspond to the boundary of A_Δ. Similarly, we can discretize the set B and use a discrete subset B_Δ for its representation. Approximations of the δ-*parallel* body of A and B can be obtained by considering their discrete representation A_Δ and B_Δ. Let $A_{\Delta\delta}$ be the δ-*parallel* body constructed from A_Δ; let $B_{\Delta\delta}$ be the δ-*parallel* body constructed from B_Δ. Finally, we can approximate the HD distance with:

$$HD(A_\Delta, B_\Delta) = \inf\{\delta : A_\Delta \backslash B_{\Delta\delta} = \emptyset \text{ and } B_\Delta \backslash A_{\Delta\delta} = \emptyset\}. \tag{11}$$

Expression (11) derives from Eq. (7). As far as we know, (11) has not be used before to compute *HD*. In next section, we show how the δ-*parallel body* can be efficiently computed for digital image.

3.1. Generation of the δ-parallel body by mathematical morphology

By replacing Eq. (7) with Eq. (11), we can simplify the traditional algorithm for calculating the HD between two digital images. Moreover, in this section we present some considerations using (11) that can render its computation on discrete images even more intuitive and simple.

Let D_Δ be a discrete domain (portion of R^2 where our images are represented). Let A_Δ and B_Δ be two digital sets (see Fig. 4(e)). These sets can be represented as binary images, where each pixel presents only two possible states **1** (turn on) representing its pixels and **0** (turn off) representing the background. Mathematical Morphology (MM) is a branch of Digital Image Processing, which uses concepts of set theory as intersection, union, complement, difference, inclusion and reflection on the construction of its main operations: dilation, erosion [21]. In binary MM, an image is viewed as a subset of D_Δ [18]. The basic idea in binary MM is to operate on an image with a simple, pre-defined shape called *structuring element* (denoted by E), that is itself a binary image with origin at a defined point; say (x_{1o}, x_{2o}). Fig. 5(a) shows some structuring elements. When an E presents a center of symmetry it is usual to consider this position as its origin. Two widely used structuring elements are squares and disk of radius δ and center in (x_{1o}, x_{2o}).

Definition. Suppose that A_Δ is a subset of D_Δ, corresponding to a binary image, and that E is a symmetrical structuring element. Let E_x denote the translation of E so that its origin is at x in D_Δ. Then the **dilation** of A_Δ by E is simply the union of all points y of E_x when x is any point in A_Δ [21].

In order to compute the dilation of a binary image by a structuring element, we consider the *background* pixels in the border of the image. For each background pixel x we superpose E so that the origin of the structuring element (its center in the case of *circular structuring element*) coincides with x. If *at least one* pixel in E coincides with a pixel of the image, then x is set to the foreground value. If there is no coincidence, x is left at the background value [18].

Please cite this article in press as: A. Conci, et al., A new measure for comparing biomedical regions of interest in segmentation of digital images, Discrete Applied Mathematics (2015), http://dx.doi.org/10.1016/j.dam.2015.06.002

The final shape of the dilation is related to E, it defines the local neighborhood of A_Δ that must be included in its dilation. Then for square E, local neighborhoods of A_Δ look like squares (Fig. 5(c) and (g)), and for disks, they look like circles (Fig. 5(d) and (h)). Therefore, the morphological operation of *dilation of* A_Δ for a *disk of radius* δ presents the same *local neighborhoods* of the Euclidean norm d_2, in R^2.

Proposition. *Consider a discrete subset A_Δ of (R^2, d_2), where $d_2 = ((x_1 - y_1)^2 + (x_2 - y_2)^2)^{1/2}$. The dilation of A_Δ for a circular structuring element of radius δ coincides with the δ-parallel body of A_Δ.*

Proof. This is immediate from (6) and the definition of dilation of a subset of D_Δ.

This proposition induces the new algorithm used to compare the distance between digital images.

3.2. Computing HD by using the geometry of the parallel body

By considering the results in Section 3.1, the problem of finding the *HD* between subsets of D_Δ can be replaced by the one of finding the radius δ of the structuring element to promote the proper dilation of the sets. According to the expression (7), δ_A is the smallest radius δ of structuring element E that makes the dilation of A_Δ by E covers B_Δ, and δ_B is the smallest radius δ *of* E that makes the dilation of B_Δ by E covers A_Δ. Then, the *HD* between the sets is the greatest between δ_A and δ_B. A simple algorithm to calculate δ is described in the following, where D_Δ is the discrete portion of R^2, where points are represented by 0's and 1's:

1 - Set HD=0, $\delta_A = 0$, $\delta = 0$, $\boldsymbol{t} = 0$.
2 - Consider A_Δ and B_Δ represented by pixels of values **1**.
3 - Compute δ_A by:
  3.1 - Compute the dilation of A_Δ for a ***disk*** with increasing radius $\boldsymbol{r}$.
  3.2 - Turn the dilated region to **0** (that is turnoff its pixels).
  3.3 - Repeat 3.1 and 3.2 until there is ***nopixel*** with value **1** (turn on).
4 - Set $\delta_A = \boldsymbol{r}$ and $\boldsymbol{t} = \boldsymbol{t} + \mathbf{1}$.
5 - If $\delta_A > \delta$ then $\delta = \delta_A$.
6 - HD $= \max\{\text{HD}, \delta\}$.
7 - Repeat from step 3 by inverting the roles of sets A_Δ and B_Δ.
8 - End.

This algorithm can be used for computation of the *HD* of discrete images. In comparison with other algorithms in the literature, this is a simpler algorithm and more intuitive for computing the *HD* between two digital images. Moreover, since the computation of the dilation can be optimized on GPUs [20] our algorithm can be extremely efficient computationally. In fact, all other algorithms compute the *HD* as the greatest distance from one point to a set of points [1], which is much more computationally expensive [13].

3.3. A new measure for comparing ROI

Section 3.2 presented a new algorithm to calculate *HD*. However, as the results of the next section show, this and all the measures in Section 2 have drawbacks, when used to compare segmented images for ROI evaluation. These drawbacks highlight the need for a new measure to pair with the physician's expectation when examining an organ and at same time the CADs requisites. In order to illustrate, these we use a group of synthetic images.

In the following, suppose that the D_Δ is a square made from the Cartesian product of the interval $[-0.2, 1.2]$ by itself with resolution 0.1 (i.e. $\{-0.2, -0.1, \ldots, 1.1, 1.2\} \times \{-0.2, -0.1, \ldots, 1.1, 1.2\}$). Sets A_Δ and B_Δ are made by taking the union of small squares of 0.1×0.1 as shown in the drawings on Fig. 6. For instance, for the Case 1 in Fig. 6 they are:

$$A_\Delta = \{(x_1, x_2) : x_1, x_2; \in \{0.0, 0.1, 0.2, \ldots, 0.8, 0.9, 1.0\}\};$$
$$B_\Delta = \{(x_1, x_2) : x_1, x_2; \in \{0.1, 0.2, 0.3, \ldots, 0.9, 1.0, 1.1\}\}.$$

PR frequently deals with shape estimation. In this case, the ROIs are correctly defined for the Cases 1, 2 or 3 in Fig. 6. In cases where area or length must be evaluated, variation between Case 1 and 3 must be considered. However, in medical analysis, it is expected that the selected set has a proper definition of the inside area; because in this set there is an expectation for information to be extracted by using the proper image analysis techniques associated with the set.

The inclusion of relevant aspects of the tissues or organs in analysis is much more important than small details related to irregularity of the borders. In biomedical considerations, border is more related to the coarser level, multi-scale and multi-resolution representation of the image. In CADs segmentation, irregularity can be related to the resolution or scale of the images under consideration, and they are not so important [8]. In medical analysis, Case 4 presents better segmentation than Case 3 and Case 1. Case 5 and 6 are better than Case 4. Case 7 is better than Case 8, and both are better than Cases 4, 5 and 6. All the area of an organ must be included. Occurrence of *FN* and *FP* must be minimal. Moreover, the existence of *FP* in some cases can be better than the presence of *FN*.

Please cite this article in press as: A. Conci, et al., A new measure for comparing biomedical regions of interest in segmentation of digital images, Discrete Applied Mathematics (2015), http://dx.doi.org/10.1016/j.dam.2015.06.002

Fig. 6. Possible ROI definition by a given method (red lines) and its relation with the correct ROI (green lines). The white area represents the TP region. The gray area represents the *TN* region. The yellow area represents the *FN* region. The blue area represents the *FP* region. (For interpretation of the references to color in this figure legend, the reader is referred to the web version of this article.)

The use of overlapping measures implies on the employment in the evaluation of the measures in Eqs. (1) to (5). The use of several values makes the evaluation very complex. The measure being a single value makes it easily verified during examination, but it must match properly all the expectations. Moreover, the notion of zero values being the best possible and that larger results correspond to the most different measures is intuitively satisfying. We consider proper combinations of overlap measures in order to have adequate conditions that only one number is able to condense all of this information consistently. After all possible experimentation, using such measures, we propose a combination from (1), (4) and (5), and we state that we can have confidence measure of the region for use in medical evaluation of segmentation results in PR with:

$$ROI\text{-}Index = 100 * (1 - ACC * PDN * PDP). \tag{12}$$

This index was developed on the basis of what it is expected to be in a ROI for medical purpose. For tumor detection, the accuracy and the predictive measures (Eqs. (1), (4), (5)) of the results are much more relevant than the sensitivity and specificity (Eqs. (2), (3)). These two are presented in the *EFI* and *Y-index*, and, they do not differentiate properly among ROI segmentations. Eq. (11) shows better relationship to human expectation, where a smaller value presents a better result. To make the index more related to the usual perception of distance (i.e. least values present closer results) it is subtracted from 1, and in order to be represented in percentage, it is amplified 100 times (making the changes more perceptible). The ROI-index in Eq. (12) is able to provide more reliable comparisons between digital images, even better than the standard *HD*, as shown in the next section.

4. Outcomes

Fig. 6 shows synthetic sets. Cases a to f are variations of Case 2, where the areas have a common *HD* but with different values for CAD systems. The boundaries of sets A_Δ and B_Δ in these change ±0.01 as represented from Case a to Case f, and

Please cite this article in press as: A. Conci, et al., A new measure for comparing biomedical regions of interest in segmentation of digital images, Discrete Applied Mathematics (2015), http://dx.doi.org/10.1016/j.dam.2015.06.002

Table 1
Results for Case 2 and a to f of Fig. 6.

Measure	Case 2	Case a	Case b	Case c	Case d	Case e	Case f
Area of TP	1	1	0.99	0.99	1	0.99	1
Area of TN	1	0.43	0.44	0.44	0.43	0.42	0.44
Area of FN	0	0	0.01	0.01	0.01	0.01	0
Area of FP	0	0.01	0	0	0	0.01	0
ACC	1	0.993	0.993	0.993	0.993	0.986	1
SEN	1	1	0.990	0.990	0.990	0.990	1
ESP	1	0.977	1	1	1	0.977	1
EFI	1	0.989	0.995	0.995	0.995	0.983	1
PDP	1	0.990	1	1	1	0.990	1
PDN	1	1	0.978	0.978	0.977	0.977	1
Y-index	1	0.977	0.990	0.990	0.990	0.967	1
ROI-index	0	1.678	2.901	2.901	2.951	4.655	0

Table 2
Results for the images of the group 1 of Fig. 7. In opposition of the other results, those with smaller ROI-index and HD indicate that the segmentation looks closer to its GT.

Measure	IR_3830		IR_5986		IR_7464		IR_8228	
Seg.Tech.	LSF	BSP	LSF	BSP	LSF	BSP	LSF	BSP
ACC	0.985	0.981	0.987	0.985	0.984	0.982	0.985	0.982
SEN	0.984	0.986	0.991	0.994	0.983	0.987	0.990	0.991
ESP	0.987	0.974	0.983	0.978	0.985	0.977	0.980	0.973
EFI	0.986	0.980	0.987	0.986	0.984	0.982	0.985	0.982
PDP	0.990	0.979	0.979	0.973	0.984	0.976	0.980	0.972
PDN	0.980	0.983	0.993	0.995	0.985	0.988	0.991	0.991
HD	10.630	11.310	9.900	11.310	12.730	15.560	11.310	14.140
Y-index	0.971	0.960	0.974	0.972	0.968	0.965	0.970	0.964
ROI-index	4.388	5.690	4.101	4.553	4.685	5.309	4.421	5.421

the area of D_Δ is now considered to be:

$$D_\Delta = \{(x_1, x_2) : x_1, x_2; \in \{-0.1, 0.0, 0.1, \ldots, 1.0, 1.1\}\}.$$

Q5 Table 1 shows the proposed *ROI-index* and allthe evaluator commented for case 2 and the cases a to f of Fig. 6. It is interesting to see that: (1) Case 2 and Case f present the same value for diagnosis; (2) Configurations of "Case a" to "Case e" present different values for diagnosis; (3) Considering the relevance of *TP*, *FP* and *FN* in CADs, they are graded in the order of Case f $<$ Case a $<$ Case c $<$ Case b $<$ Case d $<$ Case e. *ACC* does not show any difference among the Cases a through d. *SEN* groups the 6 cases into only two values. *ESP* considers Case c and Case d to be equal. *EFI* considers Case a, b and e to be equal and also Case c $=$ Case d. *PDP* exhibits only 2 values for all the 7 cases, while *PDN* exhibits only 3 values for all. *Y-index* presents 4 values for the cases but, it did not distinguish Case b from Case e and Case c from Case d, moreover, the grades are in an inadequate order. The proposed *ROI-Index* is better than all those discussed above.

To compare the results of the proposed index on real images, we consider the two approaches presented by Marques and Conci [12] for automatic segmentation and its results against the GTs. The approaches developed are based on the use of the least squares fitting (LSF) or B-Spline (BSP) for definition of the breast boundaries. The *HD*, *ROI-Index* and all the overlapping measures for these are presented in Tables 2 to 4. All images can be viewed or downloaded at http://visual.ic.uff.br/en/proeng. The labels of these images correspond to the numbers of the database used, which are registered under the number CAAE 01042812.0.0000.5243 [22]. The IR image considered is identified by its number. Segmentations and GTs can be found at: http://visual.ic.uff.br/en/proeng/marques/.

All algorithms used have been implemented in C++ programming language using OpenCV libraries version 2.3.1 and GSL (GNU Scientific Library) version 1.8. For the evaluation of the ROIs, 3 GTs for each image were generated by using a Samsung Galaxy P7510 tablet with stylus screen marker. These were grouped compounding a unique GT for each image [13]. The *HD* and overlapping measures between each final GT and the ROI is computed in the same environment.

Figs. 7–9 show the images with each of the three ROI to allow better study of the *HD* and ROI-index. Let us consider 5 groups in these images: (1) the two segmentation techniques present good ROI, but one is better than the other; both (*HD* and ROI index) show this properly; (2) both techniques present bad ROI, but one is even worse than the other, both *HD* and ROI index show this; (3) the two techniques presents good ROI, but one is better than the other and only ROI-index shows this; (4) both techniques present bad ROIs, but one is even worse than the other, and only the ROI-index shows this; and (5) only one technique presents good ROI, and both *HD* and ROI-index show this.

In group 1, there are 4 images (IR_3830, IR_5986, IR_7464, and IR_8228). In these images, the LSF visual boundaries of the breast (represented by the red line) are (on average) the closest of the GT borders (green line). The results for each segmentation in this group shows, for both *HD* and the ROI-index lower values (Table 2). The same visual sensation is matched also for the ACC, ESP, EFI, PDP and Y-index.

Please cite this article in press as: A. Conci, et al., A new measure for comparing biomedical regions of interest in segmentation of digital images, Discrete Applied Mathematics (2015), http://dx.doi.org/10.1016/j.dam.2015.06.002

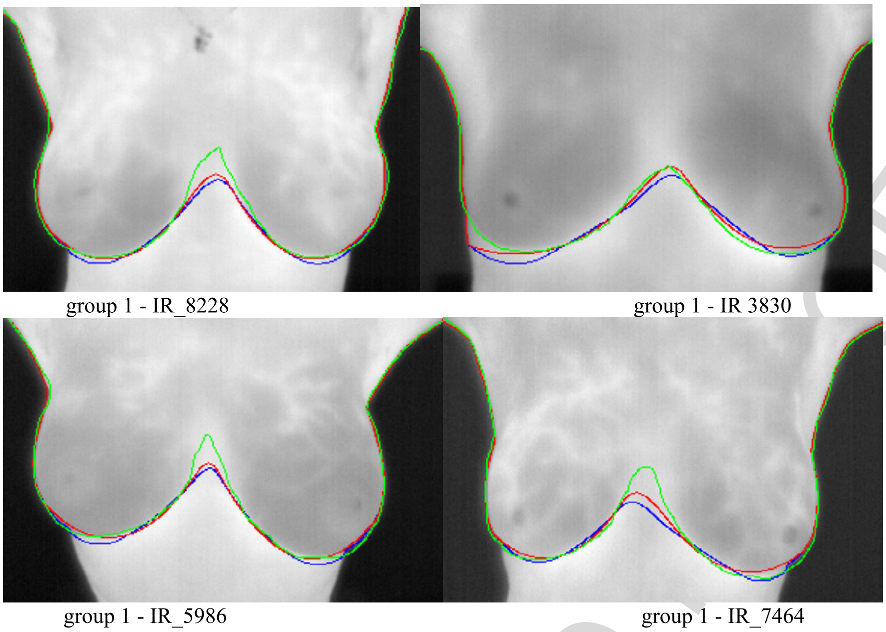

Fig. 7. ROI segmented properly (groups 1) by two techniques. The overlay of edges from segmentation by LSF technique is in red lines, by BSP technique are in blue and the GT is represented by green lines. Results of the computed measures for these are presented in Table 2. (For interpretation of the references to color in this figure legend, the reader is referred to the web version of this article.)

Table 3
Results for the images of group 2 (Fig. 8). Results with smaller *ROI-index* and HD indicate that the segmentation looks closer to its GT.

Image	IR_1252		IR_3921		IR_4875		IR_7446	
Seg.Tech.	LSF	BSP	LSF	BSP	LSF	BSP	LSF	BSP
ACC	0.968	0.967	0.971	0.966	0.959	0.935	0.967	0.959
SEN	0.950	0.952	0.996	0.995	0.997	0.996	0.999	0.999
ESP	0.984	0.982	0.947	0.937	0.915	0.863	0.928	0.910
EFI	0.967	0.967	0.971	0.966	0.956	0.930	0.964	0.954
PDP	0.982	0.979	0.949	0.940	0.931	0.894	0.945	0.932
PDN	0.955	0.957	0.995	0.995	0.996	0.995	0.999	0.999
HD	24.040	26.870	21.210	23.350	30.410	36.070	20.520	22.630
Y-index	0.934	0.933	0.942	0.932	0.912	0.859	0.927	0.909
ROI-index	9.189	9.388	8.243	9.665	11.036	16.821	8.651	10.722

Table 4
Results for the images of group 3, 4 and 5 (Fig. 9).

Measure	IR_1283		IR_1367		IR_3113		IR_5870	
Seg.Tech.	LSF	BSP	LSF	BSP	LSF	BSP	LSF	BSP
ACC	0.980	0.980	0.968	0.970	0.989	0.981	0.983	0.975
SEN	0.990	0.991	0.937	0.940	0.997	0.997	0.981	0.984
ESP	0.970	0.970	0.989	0.990	0.983	0.971	0.986	0.964
EFI	0.980	0.980	0.963	0.965	0.990	0.984	0.984	0.974
PDP	0.972	0.972	0.984	0.984	0.977	0.960	0.987	0.969
PDN	0.989	0.990	0.959	0.961	0.997	0.998	0.979	0.982
HD	16.970	17.690	21.000	22.670	11.310	15.560	7.070	18.440
Y-index	0.960	0.960	0.927	0.930	0.980	0.967	0.967	0.949
ROI-index	5.777	5.680	8.695	8.297	3.659	6.006	4.952	7.238

In group 2, there are four images (IR_1252, IR_3921, IR_4875, and IR_7446). In these, the visual boundaries of the technique LSF (represented by the red line) are the closest to the GT borders (green line). The results of segmentation in this group (Table 3) show for both *HD*, and the proposed index, lower values, although both are much higher than those of Table 2. The results of BSP are even higher, thus representing this properly. The same visual sensation is matched also for the ACC, ESP, PDP and Y-index.

In group 3, there is an image (IR_1283) where the visual boundary using the technique B-Spline (BSP) for the definition of the breast boundaries (represented by the blue line) is the closest of the GT borders (line green). The results for segmentation

Please cite this article in press as: A. Conci, et al., A new measure for comparing biomedical regions of interest in segmentation of digital images, Discrete Applied Mathematics (2015), http://dx.doi.org/10.1016/j.dam.2015.06.002

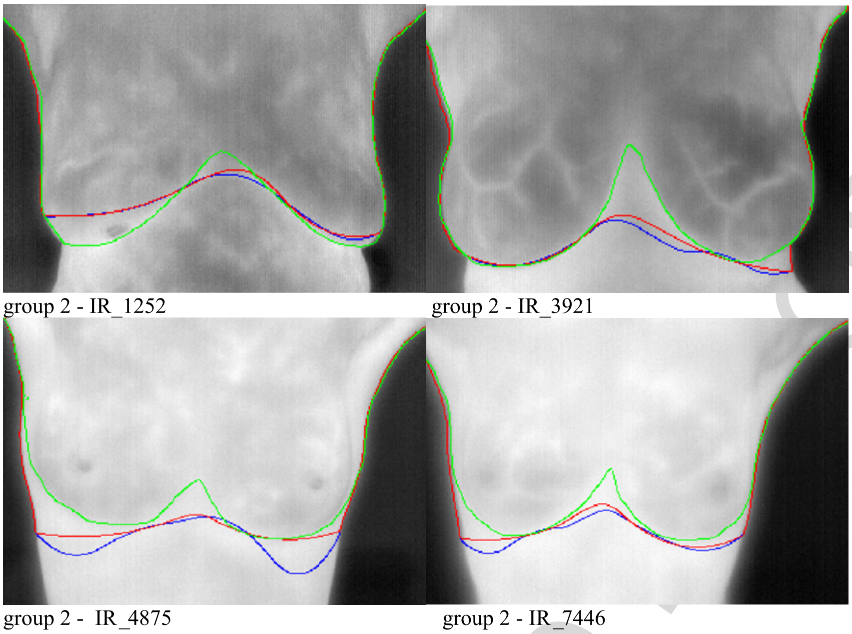

Fig. 8. Incorrect ROIs (group 2), where the segmentation border by LSF technique are in red lines, by BSP technique are in blue, and the GT is represented by green lines. Results of for these are presented in Table 3. (For interpretation of the references to color in this figure legend, the reader is referred to the web version of this article.)

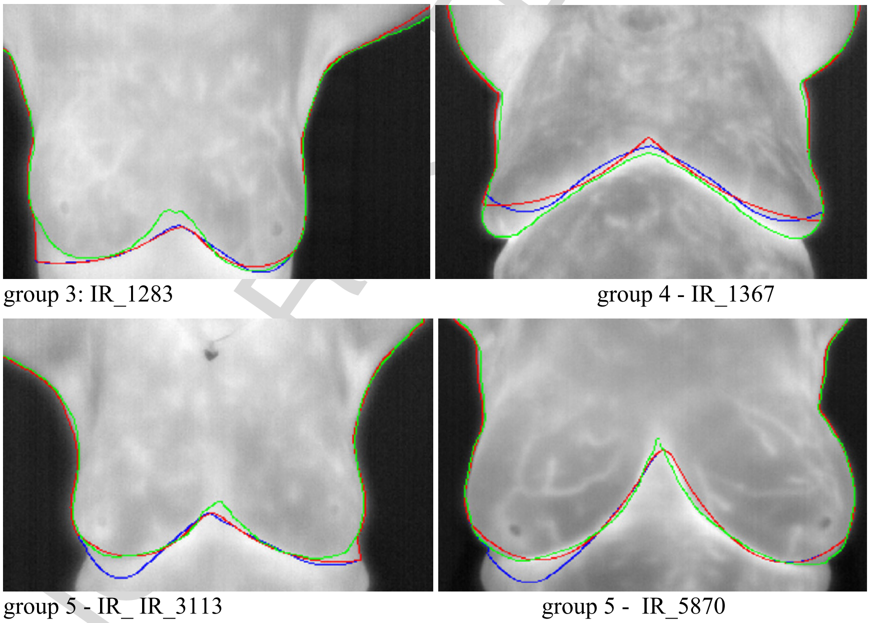

Fig. 9. Segmentations for groups 3–5 by two techniques and its GTs. Edges for segmentation by LSF technique are in red; by BSP technique are in blue, and the GT is represented by green lines. Results for these are presented in Table 4. (For interpretation of the references to color in this figure legend, the reader is referred to the web version of this article.)

in this group show opposite results for *HD* (Table 4), but, the proposed index presents lower values, that is, the *ROI-Index* is closer to what can be seen in the images. The same visual sensation is matched only for SEN and PDN.

In group 4, there is an image (IR_1367), in which the visual boundaries of the technique BSP, (represented by the blue line), are visually closer to the GT borders (green line). The results for segmentations in this group (Table 4) show opposite results only for *HD*. The proposed index and all others present the correct result, that is, BSP is closer to the GT of the images.

In group 5, there are two images (IR_3113 and IR_5870), in these the visual boundaries of the LSF technique (red line) are the closest of the GT borders (green line), the other is visually very different. This closeness (Table 4) is represented by *HD* (the proposed index and all others except PDN).

It is possible to see that a simpler and more intuitive notion of correctness of the results is obtained for the new index. This measure can be used in segmentation results in an intuitive and fast way. Moreover it is more representative for medical diagnosis than the others. It is better in a number of cases when the visual results are confronted with the various degrees of adequacy of each approach.

Comparing the results of Tables 2–4 and the ROIs in Figs. 7–9 it is possible to see that the proposed new index behaves better than the HD. As the HD provides a unique measure, its applications are simpler and more intuitive than the other evaluator. The ROI-Index makes it possible to consider that all results are good when they are lower than a threshold value (around 5.9). Moreover, this new index represents properly the segmentation results, and can be used as a measure in real time due to the very small computing time needed for its evaluation.

5. Concluding remarks

In this work, a new index for the evaluation of the correctness of the ROI segmentation is proposed, which represents the actual medical needs for diagnostics. The idea that the construction of the δ-*parallel body* of discrete sets can be seen as the morphological operation of *dilation* of the set by using a *disk* (as *structuring element*) is proposed. Moreover, a new approach for computing the *HD* is presented, which is based on the computation of the δ-*parallel* bodies of digital images.

Acknowledgments

The authors thank R. Marques for construction of the GTs, for implementation of the segmentation methods, and organization of these in a web site. Especially, we thank the reviewers and the guest editors for all the suggestions and new ideas that improve very much the original work. A. Conci thanks the Diseases Modeling Center and its director Prof. Dr. J. Wu for partially supporting the development of this work during her stay in York University, to FAPERJ Project SIADE and to the CNPq project 302298/2012-6, as well. Q6 Q7

References

[1] M.F. Barnsley, Fractal Everywhere, second ed., Academic Press, 1993.
[2] L.M. Blumenthal, Theory and Applications of Distance Geometry, second ed., Chelsea Publishing Company, Bronx, New York, 1970.
[3] T.B. Borchartt, A. Conci, R.C.F. Lima, R. Resmini, A. Sanchez, Breast thermography from an image processing viewpoint: a survey, Signal Process. 93 (2013) 2785–2803.
[4] X. Deng, L. Zhu, Y. Sun, C. Xu, L. Song, J. Chen, R.D. Merges, M.P. Jolly, M. Suehling, X. Xu, On simulating subjective evaluation using combined objective metrics for validation of 3D tumor segmentation, in: Proceedings of the Medical Image Computing and Computer-Assisted Intervention, 2007, pp. 977–984.
[5] K.J. Falconer, Fractal Geometry: Mathematical Foundations and Applications, Wiley, 1990.
[6] K. Frounchi, L.C. Briand, L. Grady, Y. Labiche, R. Subramanyan, Automating image segmentation verification and validation by learning test Oracles, Inf. Softw. Technol. 53 (12) (2011) 1337–1348.
[7] G. Gan, C. Ma, J. Wu, Data Clustering: Theory. Algorithms and Applications, SIAM, 2007.
[8] H. Jankowski, L. Stanberry, Confidence regions for means of random sets using oriented distance functions, Scand. J. Statist. 39 (2) (2012) 340–357.
[9] R. Johnsonbaugh, Discrete Mathematics, Prentice Hall, 2008.
[10] C.S. Kubrusly, Elements of Operator Theory, Birkhäuser, Boston, 2001.
[11] L. Liberti, C. Lavor, N. Maculan, A. Mucherino, Euclidean distance geometry and applications, SIAM Rev. 56 (1) (2014) 3–69.
[12] R.S. Marques, A. Conci, On the use of hausdorff distance on evaluation of breast image segmentation, in: Proceedings BIOMAT Symposium, 2013.
[13] R.S. Marques, D.A. Machado, G. Giraldi, A. Novotny, A. Conci, A new algorithm for efficient computation of Hausdorff distance in evaluation of digital image segmentation. Book of extended abstracts. Workshop on Distance Geometry and Applications, 2013, pp. 175–180.
[14] R.S. Marques, R. Resmini, A. Conci, R. Lima, C.A.P. Fontes, Método para segmentação manual de imagens térmicas para geração de Ground Truth, in: Proceedings of XII Workshop em Informática Médica, XXXII Congresso da Sociedade Brasileira de Computacao, Curitiba, CSBC WIM, 2012.
[15] C.E. Metz, Basic principles of ROC analysis, Semin. Nucl. Med. 8 (4) (1978) 283–298. (Available at: www.ncbi.nlm.nih.gov/pubmed/112681).
[16] S. Mitra, B.U. Shankar, Integrating radio imaging with gene expressions toward a personalized management of cancer, IEEE Trans. Hum. Mach. Syst. 99 (2014).
[17] A.W. Naylor, G.R. Sell, Linear Operator Theory in Engineering and Science, Rolt, Ribehart & Winston, New York, 1971.
[18] C.C. Nuñez, A. Conci, A JavaScript tool to present mathematical morphology to beginner, in: Proceedings of the 8th Intern. Symposium on Mathematical Morphology, Vol. 2, 2007, pp. 75–76.
[19] É.O. Rodrigues, A. Conci, T.B. Borchartt, A.C. Paiva, A. Correa Silva, T. MacHenry, Comparing results of thermographic images based diagnosis for breast diseases, in: IWSSIP Proceedings, 2014, pp. 39–42. Available at: http://ieeexplore.ieee.org/.
[20] A. Salgado, A. Conci, On the simulation of ocean waves in real-time using the GPU, in: XX Brazilian Symposium on Computer Graphics and Image Processing, SIBGRAPI 2007, pp. 15–16.
[21] J. Serra, Image Analysis and Matematical Morfology, Academic Press, London, 1982.
[22] L.F. Silva, D.C.M. Saade, G.O. Sequeiros, A.C. Silva, A.C. Paiva, R.S. Bravo, A. Conci, A new database for breast research with infrared image, J. Med. Imaging Health Inform. (JMIHI) 4 (2014) 92–100.
[23] S.S. Suganthi, S. Ramakrishnan, Semi automatic segmentation of breast thermograms using variational level set method, in: The 15th International Conference on Biomedical Engineering IFMBE Proceedings. Vol. 43, 2014, pp 231–234.
[24] Z. Wang, A.C. Bovik, H.R. Sheikh, E.P. Simoncelli, Image quality assessment: From error visibility to structural similarity, IEEE Trans. Image Process. 13 (4) (2004) 600–612.
[25] L. Zhang, L. Zhang, X. Mou, D. Zhang, FSIM: A feature similarity index for image quality assessment, IEEE Trans. Image Process. 20 (8) (2011) 2378–2386.

Please cite this article in press as: A. Conci, et al., A new measure for comparing biomedical regions of interest in segmentation of digital images, Discrete Applied Mathematics (2015), http://dx.doi.org/10.1016/j.dam.2015.06.002